


Article

Modelling of Microstructure Evolution during Laser Processing of Intermetallic Containing Ni-Al Alloys

Mohammad Amin Jabbareh ^{1,*} and Hamid Assadi ^{2,*} 

¹ Department of Materials and Polymer Engineering, Hakim Sabzevari University, Sabzevar 9617976487, Iran

² Brunel Centre for Advanced Solidification Technology, Brunel University London, Uxbridge UB8 3PH, UK

* Correspondence: m.jabbareh@hsu.ac.ir (M.A.J.); hamid.assadi@brunel.ac.uk (H.A.)

Abstract: There is a growing interest in laser melting processes, e.g., for metal additive manufacturing. Modelling and numerical simulation can help to understand and control microstructure evolution in these processes. However, standard methods of microstructure simulation are generally not suited to model the kinetic effects associated with rapid solidification in laser processing, especially for material systems that contain intermetallic phases. In this paper, we present and employ a tailored phase-field model to demonstrate unique features of microstructure evolution in such systems. Initially, the problem of anomalous partitioning during rapid solidification of intermetallics is revisited using the tailored phase-field model, and the model predictions are assessed against the existing experimental data for the B2 phase in the Ni-Al binary system. The model is subsequently combined with a Potts model of grain growth to simulate laser processing of polycrystalline alloys containing intermetallic phases. Examples of simulations are presented for laser processing of a nickel-rich Ni-Al alloy, to demonstrate the application of the method in studying the effect of processing conditions on various microstructural features, such as distribution of intermetallic phases in the melt pool and the heat-affected zone. The computational framework used in this study is envisaged to provide additional insight into the evolution of microstructure in laser processing of industrially relevant materials, e.g., in laser welding or additive manufacturing of Ni-based superalloys.

Keywords: laser processing; additive manufacturing; microstructure; phase-field method; intermetallics



Citation: Jabbareh, M.A.; Assadi, H. Modelling of Microstructure Evolution during Laser Processing of Intermetallic Containing Ni-Al Alloys. *Metals* **2021**, *11*, 1051. <https://doi.org/10.3390/met11071051>

Academic Editor: Antonio Riveiro

Received: 1 June 2021
Accepted: 28 June 2021
Published: 30 June 2021

Publisher's Note: MDPI stays neutral with regard to jurisdictional claims in published maps and institutional affiliations.



Copyright: © 2021 by the authors. Licensee MDPI, Basel, Switzerland. This article is an open access article distributed under the terms and conditions of the Creative Commons Attribution (CC BY) license (<https://creativecommons.org/licenses/by/4.0/>).

1. Introduction

Laser melting is the basis of various modern processing and fabrication techniques, such as laser surface alloying, laser welding and metal additive manufacturing (AM). High cooling rates, large thermal gradients, and rapid solidification in these processes often result in the formation of strong texture and metastable microstructures, which can greatly affect the performance of the fabricated parts [1–4]. In metal AM, for example, the formation of columnar grains during solidification is a common feature responsible for anisotropy in mechanical properties [5,6] and reduced fracture resistance [7]. Moreover, metal AM can be associated with further microstructural complexities, such as precipitation or dissolution of secondary solid phases in the heat-affected zone (HAZ) [8] or compositional banding in the melt pool [9].

In contrast to conventional solidification processing of metals, on the other hand, laser treatment provides a unique opportunity to control the local thermal history of the material by manipulating the process parameters, namely the energy input, the scan rate, and the spot size [10,11]. All these parameters can be linked to the local temperature gradient, cooling rate and solidification velocity, hence be used to control the resulting microstructure. It is known, for example, that the cooling rate controls the fraction of second phases [12,13] and the heat input determines the depth of HAZ [14] during laser surface treatment. Previous studies on metal AM also show that columnar-to-equiaxed transition (CET) is critically controlled by the constitutional, thermal and curvature undercooling in

the melt pool during rapid solidification [3,15]. It has also been shown how solidification morphology can influence solute segregation and lead to the formation of unwanted phases [15–17].

The focus of a large part of the previous studies in laser processing has been on the prediction and control of the grain structure. Clearly, material properties depend on various microstructural features besides the grain structure, such as the segregation pattern, phase distribution, and formation of metastable or non-equilibrium phases [18]. Therefore, the prediction of properties and process optimisation require an understanding of not only the grain structure, but also solute partitioning and (non-equilibrium) phase formation during solidification. Modelling and numerical simulation of microstructure evolution can provide a basis for this understanding [19–21]. However, modelling of microstructure becomes particularly challenging when the solidification rate is high [22], or when the solidifying phase has a complex structure, such as an intermetallic compound with order-disorder transition [23]. An example is AM of Ni-based superalloys, which involves at the same time (a) high solidification rates and (b) alloys that contain intermetallic phases. A particular challenge is that intermetallics may exhibit unusual solidification behaviour, such as anomalous partitioning [24,25], which can be very different from that of random solid solutions. These unique aspects of intermetallic solidification cannot be captured by the conventional phase-field methods.

The key problem is that when the solidifying phase shows site ordering, such as the B2 and L1₂ intermetallic phases in the Ni-Al system, the partitioning behaviour can be considerably complicated [26]. Depending on the solidification rate and the initial composition, increased partitioning, a change in the direction of partitioning or an absence of partitioning at solidification rates much lower than that required for complete solute trapping can occur [26,27]. In the Ni-Al system, for example, increasing solidification velocity results in substantial depression of the interface temperature and displacement of the congruent point to the Ni-rich side of the phase diagram [28]. These phenomena can lead to a fundamentally different solidification and microstructure evolution scenarios from what is common to random solid solutions.

There have been limited studies directed specifically at the investigation of compositional changes in laser surface treatment of intermetallic containing systems. For example, Gaffet et al. [29] investigated the mechanisms of laser surface alloying of the Ni coating of an Al-based alloy. They observed a decrease in the Ni concentration just below the surface and an increase in the Ni content in the middle of the laser passage. Liang et al. [30] showed that compositional segregation appears in the laser surface alloying of plasma sprayed coating (Ni-Cr-Al) on an Al-Si alloy. They reported a higher Al content in the surface of the laser melted zone and higher Ni and Cr contents in the inner part of the laser alloyed zone. There are overall few studies focusing on the evolution of microstructure during AM of systems containing intermetallics with an order-disorder transition—see e.g., Refs [16,31,32]—and hardly any phase-field modelling work on laser processing of such systems.

To explore the problem further, the present paper puts forward a computational framework for the simulation of partitioning and microstructure evolution during laser processing of alloys that comprise intermetallics. The focus is the intermetallic phases represented commonly by a thermodynamic sublattice model that incorporates anti-site defects, hence allowing a real (below the melting point) or virtual (above the melting point) order-disorder transition. The framework is based on the combination of a tailored phase-field model of solidification, to account for the kinetic effects during growth, including solute and disorder trapping, and a Monte-Carlo Potts model, to simulate the evolution of grain structure in the melt pool and the HAZ. Conventional phase-field models are capable of representing the growth morphology and sub-grain features, such as high-order dendrites, microsegregation and solid-state phase transformation with a reasonably high spatial resolution [33–35]. However, these models can be computationally expensive to treat multiple-grain structures. Moreover, these models are generally not suited to

model rapid solidification, especially when there is a large deviation from equilibrium at the solid/liquid interface, or when the solidifying phase is an intermetallic compound with an order-disorder transition. The phase-field model used in this work, on the other hand, incorporates chemical long-range order as an additional field variable, and can thus illustrate the non-equilibrium effects associated with solute and disorder trapping. The employed phase-field model is then combined with a Potts model of grain growth and a model of conductive heat transfer during laser melting/re-solidification. The key features of the model are demonstrated for laser processing of an intermetallic forming system, devised based on the Ni-Al binary alloy. The capability of the model to capture solute and disorder trapping is assessed in view of the experimentally observed solute redistributions in laser processed Ni-Al reported in the literature [26].

2. Method

Modelling of microstructure evolution in this work is based on a combination of a quantitative phase-field model for non-equilibrium solidification of intermetallics [23] and a probabilistic algorithm for the evolution of crystal orientation. The simulated microstructure is represented by six field variables as follows:

- i. Phase-field parameter, ϕ , which is 0 for liquid and 1 for solid.
- ii. Liquid concentration, x_B^L
- iii. Solid (Bragg-Williams) first sublattice concentration, y_B^α
- iv. Solid (Bragg-Williams) second sublattice concentration, y_B^β
- v. Temperature, T
- vi. Orientation field variable, θ .

The solid composition x_B^S and the long-range order (LRO) parameter, η , are derived from sublattice compositions by $x_B^S = \frac{1}{2}(y_B^\alpha + y_B^\beta)$ and $\eta = y_B^\alpha - y_B^\beta$, whereas the overall concentration is obtained as $x_B = \phi x_B^S + (1 - \phi)x_B^L$. The main features of the employed formalism are summarized below.

2.1. Phase and Crystal Orientation Fields

The overall free energy of the system is considered to have the following form:

$$F = \int \left[f(\phi, x_B^L, y_B^\alpha, y_B^\beta, T) + \frac{1}{2}\varepsilon^2 |\nabla\phi|^2 + g(\theta) \right] dV \quad (1)$$

where f is the local volumetric free energy density, ε is a constant relating to the solid/liquid interface thickness and $g(\theta)$ is an energy term encapsulating the free energy of the crystallographic mismatch between the given control volume (cell) and its neighbours. The local energy density is given by

$$f = h_1 G^S + (1 + h_1)G^L + h_2 W \quad (2)$$

where G^S and G^L are the Gibbs free energies of the bulk solid and liquid phases, respectively, W is the height of the energy barrier between the two phases, $h_1 = \phi^3(10 - 15\phi + 6\phi^2)$ and $h_2 = \phi^2(1 - \phi)^2$.

As described in detail in Ref. [36], the mismatch energy is given as

$$g(\theta) = \frac{1}{2}\varepsilon_0^2 \sum_i a_i \phi \phi_i |\sin[2(\theta - \theta_i)]| \quad (3)$$

where ε_0 is a constant relating to the grain boundary thickness, θ is the orientation of the given cell, i is that of its i th neighbour, and a_i is a coefficient that equals unity and $1/\sqrt{2}$ for the nearest and the second nearest neighbours in a 2-D grid, respectively.

The temporal evolution of the phase-field variable is worked out using an Allen–Cahn formulation:

$$\frac{\partial \phi}{\partial t} = -M_{\phi} \left(\frac{\partial f}{\partial \phi} - \epsilon^2 \nabla^2 \phi \right) \quad (4)$$

where M_{ϕ} is the interface mobility.

The evolution of orientation is worked out in parallel with that of other field variables through a Monte-Carlo algorithm. According to this algorithm, initially, a new orientation is generated for a given cell. Then the orientation mismatch energy between this cell and its neighbours is calculated, according to Equation (3). The probability of orientation change from the old to the new value is calculated as:

$$pr = p_0 \exp\left(-\frac{Q}{RT}\right) \left[1 - \exp\left(-\frac{k[g_{new} - g_{old}]}{RT}\right) \right] \quad (5)$$

where p_0 and k are adjustable parameters, Q is the activation energy of orientational ordering kinetics, and g_{new} and g_{old} are the mismatch energies of the new randomly generated and original orientation of the designated cell, respectively. Subsequently, a random number, r , is generated in the range 0 to 1. The new orientation is accepted if $r < pr$. Table 1 shows the parameters used for adjusting the grain growth kinetic. In this study, the parameters were set such that pr tends to zero at temperatures lower than 750 K and rapidly increases with increasing temperature. Variation of the orientation selection probability with temperature is illustrated in Figure 1.

Table 1. Grain growth kinetic parameters.

Parameter	Symbol	Value	Unit
Driving force multiplier	k	1000	–
Kinetic multiplier	p_0	50	–
Activation energy over universal gas constant	Q/R	6000	K

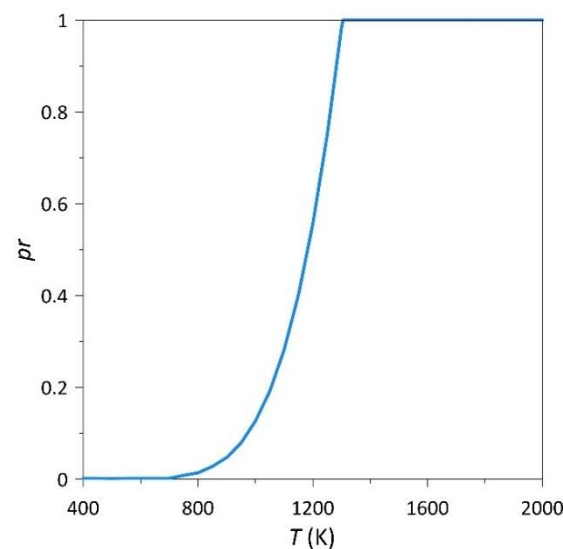


Figure 1. Variation of the new orientation selection probability with temperature, as considered for the simulations of polycrystalline microstructures.

2.2. Concentration Fields

Temporal evolution of the concentration fields was modelled using the system of equations similar to that described in Ref. [23], in which the rate of change of sublattice compositions is considered as

$$\frac{\partial y_B^j}{\partial t} = \text{sgn}(x_B^s - y_B^j) k_o h_3 F_\eta - \nabla \cdot J_0^s - \frac{1}{\phi} \left[|\nabla \phi| J^{j/l} - (y_B^j - x_B^l) \frac{\partial \phi}{\partial t} \right] \quad (6)$$

where j denotes the sublattice type, k_o is a mobility factor representing the degree of ordering kinetics, $h_3 = \phi^2(3 - 2\phi)$, F_η is the thermodynamic driving force for chemical ordering, J_0^s is the flux of solute atoms in the solid, and $J^{j/l}$ is an internal atomic flux component, representing the rate of exchange of the solute atoms between sublattice j and the liquid in the interfacial region.

The liquid composition, x_B^l , is deduced from the overall mass-conservation equation, which is given by

$$\frac{\partial x_B}{\partial t} = -\nabla \cdot J \quad (7)$$

where $x_B = \phi x_B^s + (1 - \phi) x_B^l$, and J is the overall mass flux, which is assumed to consist of two parts, $J = J_0 + J_{xs}$, where J_0 is given by

$$J_0 = \phi J_0^s + (1 - \phi) J_0^l \quad (8)$$

in which J_0^s (J_0^l) is atomic mass flux in the solid (liquid) phase which is defined as

$$J_0^{s/l} = -M_c^{s/l} \nabla \mu^{s/l} \quad (9)$$

where $\mu^{s/l} = \partial G^{s/l} / \partial x_B^{s/l} - \varepsilon_c^2 \nabla^2 x_B^l$ is the difference between the chemical potentials of the two constituents in the solid (liquid) phase and $M_c^{s/l}$ is the mobility coefficient related to solute diffusivity as $M_c^{s/l} = D^{s/l} / RT$. J_{xs} is an anti-trapping term which is described as Ref. [23]

$$J_{xs} = \frac{\partial \phi}{\partial t} (x_B^s - x_B^l) \frac{\nabla \phi}{|\nabla \phi|^2} \quad (10)$$

It should be noted that, in contrast to anti-trapping terms commonly used in conventional phase-field models, the above term is a diffuse-interface form of the Stefan problem, hence it does not contain any adjustable parameters. An important characteristic of the present model is that the composition of the interface is represented by two concentration variables, corresponding to solid and liquid, and that the diffusive reactions at the interface are governed by the sharp-interface models of partitioning. In this way, the artificial solute-trapping associated with the conventional phase-field methods is fully eliminated and the partitioning behaviour is completely controlled by the sharp-interface formulation of diffusion. This also means that the model is applicable to any growth velocity, from near-equilibrium solidification to complete solute trapping in rapid solidification, irrespective of the assumed interface thickness [23].

2.3. Temperature Field

The rate of the temperature change is calculated according to

$$\partial T / \partial t = \alpha \nabla^2 T + \dot{q} + \frac{1}{c_{pa}} \left(\frac{\partial H_{tr}}{\partial t} \right) \quad (11)$$

where α is the thermal diffusivity, \dot{q} is the heating rate. c_{pa} is the average heat capacity, and H_{tr} is an enthalpy parameter calculated as follows:

$$c_{pa} = (1 - x_B) c_p^A + x_B c_p^B \quad (12)$$

$$H_{tr} = (1 - h_1)G_{xs}^l + h_1(G_{xs}^s - L) \quad (13)$$

where c_p^i is the heat capacity of component i , $L = (1 - x_B)L_A + x_B L_B$ in which L_i is the latent heat of fusion of i component, $h_1 = \phi^3(10 - 15\phi + 6\phi^2)$ and G_{xs}^s and G_{xs}^l are the excess free energies of the solid and liquid phases, respectively.

The thermal cycle of laser processes is applied to the system as a heat flux boundary condition on the top surface of the simulation domain. In all simulations temperature of the bottom surface was fixed to 300 K while symmetric thermal boundary conditions were used for other boundaries.

2.4. Thermodynamic Model

In this work, a simplified thermodynamic model is used to represent the Ni-Al system. The liquid, the solid solutions, and three intermetallic phases (Ni-Al, Ni₃Al and Ni₂Al₃) are considered. The Ni-Al (β) phase is considered as the ordered version (B2) of the Ni-Al random solid solution (bcc) phase. This means that the overall free energy of the intermetallic formation is represented solely by the free energy of mixing and chemical ordering. The free energy of the solid solution and the liquid phase is expressed by a regular solution model as $G = G_{ref} + G_{id} + G_{xs}$ in which $G_{ref} = (1 - x_B)G_A^0 + x_B G_B^0$ is the weighted average over the composition of the Gibbs free energies of the pure elements. the Gibbs free energies of the pure elements in the solid-state are obtained with reference to that in the liquid state (i.e., $G_A^{0,l} = G_B^{0,l} = 0$) as $G_i^{0,s} = L_i(T - T_m^i)/T_m^i$, where L_i is the latent heat of fusion and T_m^i is the melting temperature of i element respectively. G_{id} is the ideal free energy of mixing which is given by $G_{id} = RT[x_B \ln x_B + (1 - x_B) \ln(1 - x_B)]$ and $G_{xs} = \Omega x_B(1 - x_B)$ represents the excess free energy in which Ω is the interaction parameter. For the β phase these components are given as follows:

$$G_{ref}^\beta = (1 - x_B^s)G_A^{0,s} + x_B^s G_B^{0,s} \quad (14)$$

$$G_{id}^\beta = \frac{RT}{2} \sum_{i,j} y_i^j \ln(y_i^j) \quad (15)$$

$$G_{xs}^\beta = \frac{\Omega_s}{2} (y_B^\alpha + y_B^\beta - 2y_B^\alpha y_B^\beta) \quad (16)$$

where y_i^j is the site fraction of i atoms on sublattice j . The two additional stoichiometric compounds, Ni₂Al₃ and Ni₃Al, are incorporated into the model by mounting two energy ditches of specific depth, δg_1 and δg_2 , on the above free energy variation, at the respective compositions of $x_B^i = 0.4$ and 0.75 . This is implemented as follows:

$$G^s = G^\beta + \delta g_i \left[1 - \left(\frac{x_B^s - x_B^i}{\delta x_B} \right)^2 \right]^2 \quad \text{if } |x_B^s - x_B^i| \leq \delta x_B \quad (17)$$

$$G^s = G^\beta \quad \text{if } |x_B^s - x_B^i| > \delta x_B$$

where the subscript $i = 1, 2$ indicates the stoichiometric compounds Ni₂Al₃ and Ni₃Al, respectively, and $\delta x_B = 0.333$ represents the width of the energy ditch, which relates to the width of the homogeneity range of the respective compound. The thermodynamic parameters used in this work are given in Table 2. The thermodynamic properties of the model system are optimized mainly with reference to the β /Liq. equilibrium in the real Ni-Al system.

Figure 2 shows the calculated phase diagram of the Ni-Al model system, which fits the real Ni-Al system particularly well around the congruent melting point of the B2 (Ni-Al) phase. Based on this phase diagram, the congruent melting occurs at $x_{Ni} = 0.506$ ($x_{Al} = 0.494$). As can be seen in Figure 2, equilibrium solidification of alloys with lower concentrations results in the rejection of Ni from liquid to solid, and vice versa.

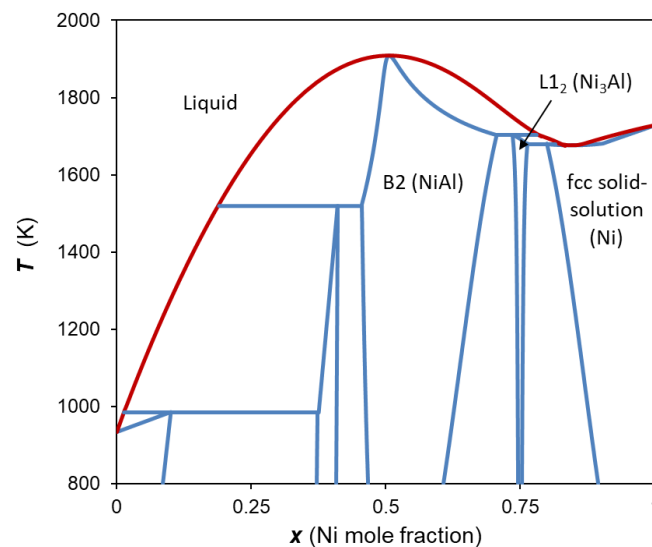


Figure 2. The calculated phase diagram for the model Ni-Al system.

Table 2. Thermodynamic parameters. The latent heats of fusion are from Ref. [37], the other parameters are from Ref. [38].

Parameter	Symbol	Value	Unit
Melting temperature	T_m^{Al}	933.5	K
	T_m^{Ni}	1728	
Interaction parameters	Ω_s	−80,000	J/mol
	Ω_1	−75,500	
$\beta \rightarrow Ni_2Al_3$ free energy	δg_1	−300	J/mol
$\beta \rightarrow Ni_3Al$ free energy	δg_2	$-800 + 0.00025 T^2$	J/mol
Heat capacity	c_p^{Al}	35.5	10^6 J/K/mol
	c_p^{Ni}	59.6	
Latent heat of fusion	L_{Al}	1070	10^6 J/m ³
	L_{Ni}	2608	

2.5. Numerical Simulation

Numerical simulations were carried out for two cases of laser surface processing of alloys in the model Ni-Al system:

1. Stationary laser melting of a single-crystalline alloy within the homogeneity range of the Ni-Al intermetallic phase, to capture and predict anomalous partitioning effects during rapid solidification of a single intermetallic phase.
2. Scanned laser melting of a polycrystalline nickel-rich alloy within the Ni-Ni₃Al two-phase region, to illustrate the effect of laser processing on the grain structure, segregation and phase distribution, both in the melt pool and in the HAZ.

In the first case, simulations were carried out for melting by stationary heat input (pulsed laser melting). In the second case, the heat input moved at a constant velocity in the horizontal direction with respect to the specimen (continuous laser melting). An explicit, isotropic finite difference scheme as implemented in the PhasePot software (Kinetic Spray Solutions GmbH, Buchholz, Germany) was employed to simulate the temporal evolution of the phase, temperature, and concentration fields. All simulations were performed on a rectangular grid with 600×150 cells. The initial temperature of the system was set to 300 K in all simulations.

In the case of stationary laser melting, simulations were carried out for alloys with three compositions of 0.35, 0.5 and 0.55 Al mole fraction, for different values of the diffusive speed ($v_d = 0.1$ to 5 m/s). The diffusive speed is a material property defined as the ratio of the solute diffusivity to the atomic jump distance [23]. This quantity relates to characteristic

solidification speeds where the growth kinetic effects—namely solute trapping and disorder trapping—become prominent. Simulation domains consisted of a single crystal solid phase with uniform initial composition. Symmetric boundary conditions were applied to all boundaries in the phase and concentration fields, except for the phase-field variable at the top boundary, which was set to zero (liquid) to allow for the initiation of melting. The thermal cycle for the single pulsed laser was applied as a heat flux boundary condition on 200 cells at the top boundary, with a power density of 6×10^4 MW/m² and a duration of 1×10^{-5} s.

Scanning laser melting simulations were carried out on a polycrystalline Ni-Al alloy with 0.2 Al mole fraction ($x_{\text{Ni}} = 0.8$). To create the initial microstructure for these simulations, isothermal solidification of the alloy was simulated in the first step. The initial condition in the isothermal solidification simulation consisted of randomly distributed solid seeds with random crystal orientations embedded in a liquid matrix with a homogeneous concentration field. The initial temperature was set to 1200 K and symmetric boundary conditions were applied to all boundaries for all field variables. The simulated microstructure (represented by the phase, concentration, and the long-range order fields) from the isothermal solidification step was subsequently used as the initial condition for the next step, i.e., simulation of laser melting. To emulate the thermal cycle of the moving heat source in the continuous melting case, a heat-flux was applied to 20 cells at the top boundary, while the calculation domain was shifted to the right with a constant velocity. To illustrate the effect of process parameters on microstructure evolution, simulations were carried out with three different laser powers (15, 21 and 27 GW/m²) corresponding to three scanning speeds (0.5, 0.7 and 0.9 m/s). In this way, the ratio of laser power densities over scanning speeds remained constant, so that the overall heat input per unit volume of material was the same in all simulations (30 GJ/m³). Other parameters used for the calculations are given in Table 3. The diffusive speed was tuned by using the same value of solute diffusivity (in liquid) and adjusting the atomic jump distance to the appropriate level to obtain the required values of $v_d = 0.1$ to 5 m/s.

Table 3. Input parameters used for numerical simulations. Solute mobilities and thermal diffusivities are from Refs [30] and [38], respectively.

Parameter	Symbol	Value	Unit
Solute mobility	M_c^s	1.2×10^{-16}	m ⁵ /J/s
	M_c^l	1.2×10^{-13}	
Thermal diffusivity	α^s	2.03×10^{-5}	m ² /s
	α^l	2.03×10^{-5}	
Solid/liquid interface energy (nominal)	σ	0.1	J/m ²
Solid/liquid interface thickness	δ	1200	nm
Interface mobility	M_ϕ	0.01	m/s/K
Ordering kinetic coefficient	k_o	100	mol/J/s
Mesh spacing	Δx (Stationary)	800	nm
	Δx (Scanned)	1500	
Time increment	Δt (Stationary)	5	ns
	Δt (Scanned)	20	

3. Results and Discussion

3.1. Stationary Laser Melting of Ni-Al

Figure 3 shows the distribution of Al concentration at the end of laser processing for three cases.

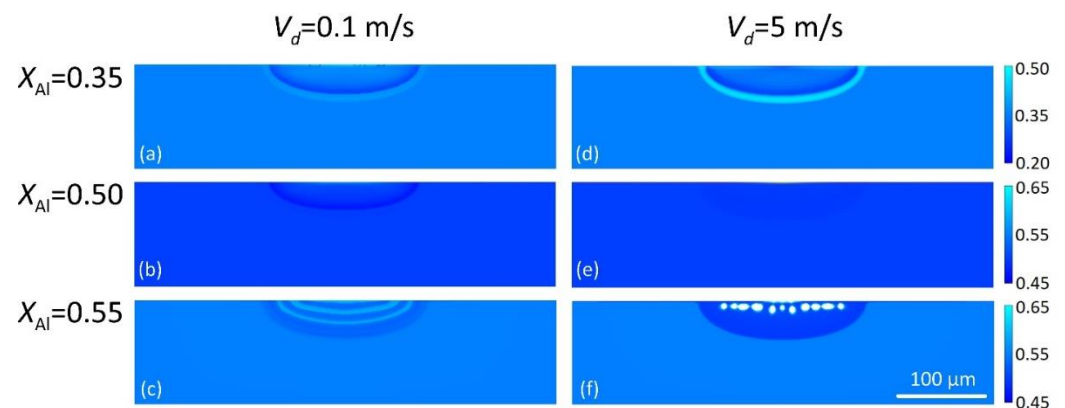


Figure 3. Final 2D distribution of Al concentration after laser surface melting, calculated for three compositions— $x_{\text{Al}} = 0.35$ (a,d), 0.5 (b,e), 0.55 (c,f)—considering two different values of the diffusive speed—0.1 m/s (a–c), 5 m/s (d–f). The white spots in (f), indicate regions with a concentration greater than the upper limit of the display range (i.e., $x_{\text{Al}} > 0.65$).

As can be seen in the figure, the concentration field is not uniform within the resolidified zone, except for one case: $x_{\text{Al}} = 0.5$, $v_d = 5$ m/s. In this case, the initial composition is close to the congruent point and the diffusive speed is one order of magnitude larger than the solidification velocity—which ranges from 0 at the bottom of the melt pool to a maximum at an intermediate distance from the bottom and then drops back to zero at the end of solidification (Figure 4a). As a result, the kinetic effects due to disorder trapping are negligible and there is congruent solidification (without partitioning). However, for the same composition but smaller values of the diffusive speed ($v_d = 0.1$ m/s in this case), solidification takes place with some partitioning. This unusual behaviour is because of disorder trapping, which is associated with and manifested by a non-zero partitioning at the congruent melting composition and is exclusive to intermetallic phases with order/disorder transition.

The two other cases with $v_d = 5$ m/s manifest partitioning according to the equilibrium phase diagram, whereas partitioning with $v_d = 0.1$ m/s appears quite different from the near-equilibrium cases. For the case of $x_{\text{Al}} = 0.35$, the partitioning scenario changes drastically when the diffusive speed is reduced, indicating a strong kinetic effect. For the case of $x_{\text{Al}} = 0.55$, the reduction of the diffusive speed leads not only to anomalous partitioning but also to compositional banding. The banding can be attributed to the fluctuation of the growth velocity and its interplay with the velocity-dependent partitioning coefficient. These examples show clearly that the employed phase-field model can appropriately capture the complex kinetic effects associated with rapid solidification of intermetallic phases.

The effect of disorder trapping on the partitioning behaviour of the B2 phase is illustrated schematically in Figure 4b. At increased growth velocities, the solidifying intermetallic phase becomes chemically less ordered as compared to the equilibrium phase. This is due to concurrent solute trapping on two sublattices, leading to a deviation of the sublattice compositions from their equilibrium values. As a result, with increasing the growth velocity, the thermodynamic properties of the solidifying phase, which depend on the sublattice compositions, will approach those of the disordered (unstable bcc random solid solution) version of the B2 phase. This effect leads inevitably to a change in the partitioning behaviour, from that of the ordered B2 to the disordered bcc phase (Figure 4b). The combination of this unique velocity-dependent partitioning with the variable growth velocity (Figure 4a) can lead to a complex segregation pattern, examples of which are illustrated in Figure 5.

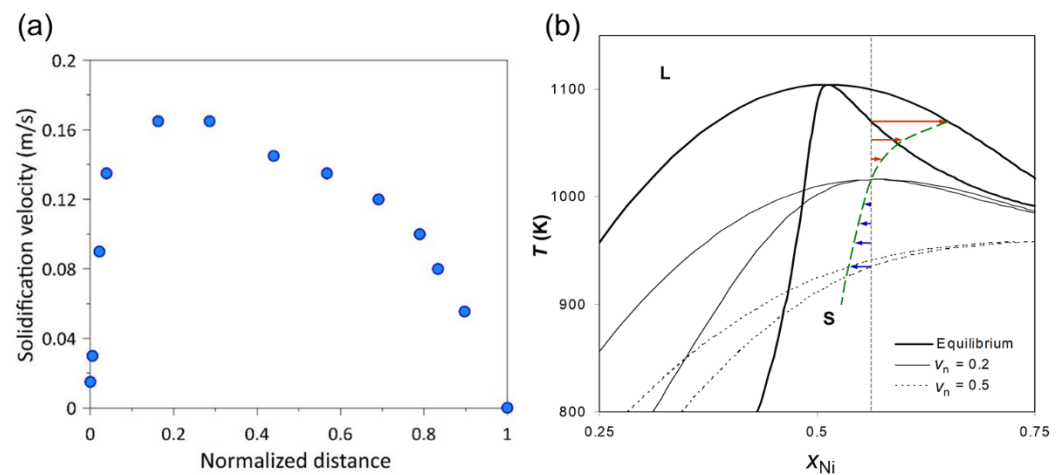


Figure 4. (a) Solidification velocity versus normalized distance from the bottom of the melt pool, calculated a system with $x_{Al} = 0.35$ ($x_{Ni} = 0.65$) and $v_d = 0.2$ m/s, and (b) schematic representation of the kinetic phase boundaries the B2 phase in a model system, indicating inversion of partitioning for an off-stoichiometric composition with increasing the normalised velocity ($v_n = v/v_d$) from 0 (equilibrium) to 0.5.

Figure 5 provides a quantitative description of these partitioning behaviours along the centreline of the melt pool. As can be seen in Figure 5c, for $x_{Al} = 0.55$, the profiles show a gradual decrease in Ni concentration in the solid, particularly in areas close to the sample surface. The segregation of Ni also decreased with decreasing diffusive speed due to a more profound kinetic effect (solute and disorder trapping). At the congruent point (Figure 5b) with a high diffusive speed, no partitioning can be detected. However, with increasing the solidification rate, segregation appears in the re-solidified zone. For higher concentrations (Figure 5a), the situation is more complex. At the high diffusive speeds ($v_d = 5$ m/s), the concentration profile is like that expected from the equilibrium solidification conditions, which includes rejection of Ni from solid to liquid. As a result, the Ni concentration reaches its maximum value on the surface of the sample. At lower diffusive speeds, in areas close to the substrate, a gradual increase of Ni concentration is observed, like that obtained during equilibrium solidification. With the progress of solidification, however, this trend is reversed, indicating the inversion of partitioning [34]. The inversion of partitioning is unique to intermetallic phases and is due to the disorder trapping effect. As the solidification velocity increases, this effect becomes more prominent. Disorder trapping is manifested by a continuous deviation from the equilibrium phase diagram (of a fully ordered intermetallic) to non-equilibrium phase boundaries (of a fully disordered solid solution). Likewise, solidification of an intermetallic phase at the congruent melting (stoichiometric) composition can exhibit increased partitioning with increasing the solidification velocity. This behaviour is unique to intermetallics and not observable in the solidification of random solid solutions, as described in more detail in Ref. [28].

Figure 6 shows the comparison between the calculated and the measured concentration profiles for the case of single-crystalline Ni-Al samples. The experimental results are related to pulsed laser surface melting of Ni-Al samples with nominal compositions of 35 and 50 at. % Al. The chemical composition change from the surface to the depth of the re-solidified zone was measured by using EDS. Details of the experiments are reported in Ref. [26]. The similarities between the experimental and simulated profiles are encouraging. The difference in the absolute values of segregation can be attributed to several factors, including convection and material evaporation, which are not considered in these simulations. The results clearly demonstrate the capability of the employed phase-field model in capturing the complex kinetic features and segregation patterns, including inversion of

partitioning [26] and compositional banding [39], which can have a significant impact on the microstructure evolution and final properties of the processed material.

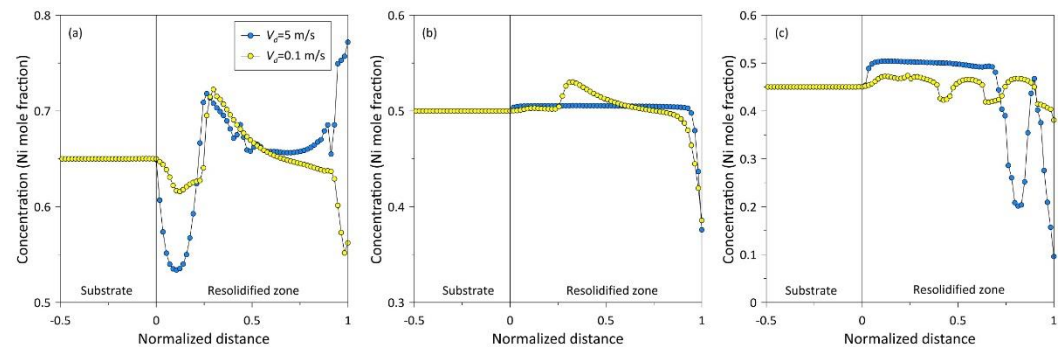


Figure 5. Concentration profile along the centreline of the melt pool for various diffusive speeds and initial compositions: (a) $x = 0.65$ (b) $x = 0.50$ Ni and (c) $x = 0.45$ mole fraction of Ni.

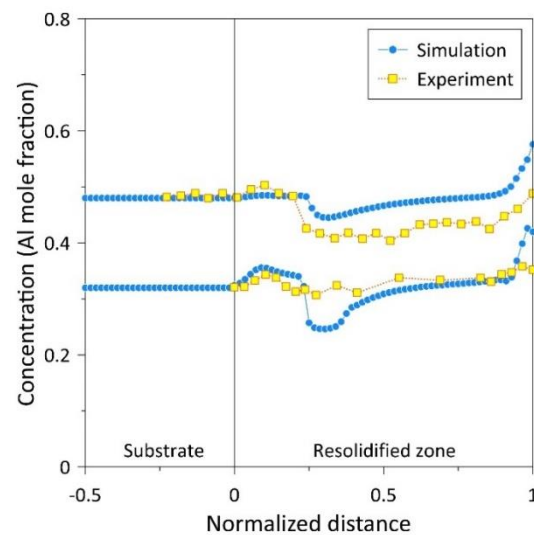


Figure 6. Comparison of the calculated (this work) and experimentally measured (literature, Ref. [26]) Al concentration along the centre line of the melt pool.

3.2. Scanning Laser Melting of Ni-Ni₃Al

Figure 7 shows the simulated grain structure and temperature distribution during laser surface melting of a polycrystalline Ni-0.2Al alloy with different laser powers and scanning speeds, but constant heat input. As can be seen from the figure, despite using a fixed input heat, changes in the process parameters result in different temperature fields and microstructure evolution paths. According to these results, increasing the scanning speed at a constant heat input reduces the depth and extends the length of the melt pool. Figure 7a–c illustrates how columnar grains grow epitaxially from the substrate to the melt pool. It is also observed that increasing the scanning speed increases the tendency of the grains to grow perpendicular to the surface. In all three cases, there is an indication of competitive grain growth (indicated by white markers in Figure 7a–c).

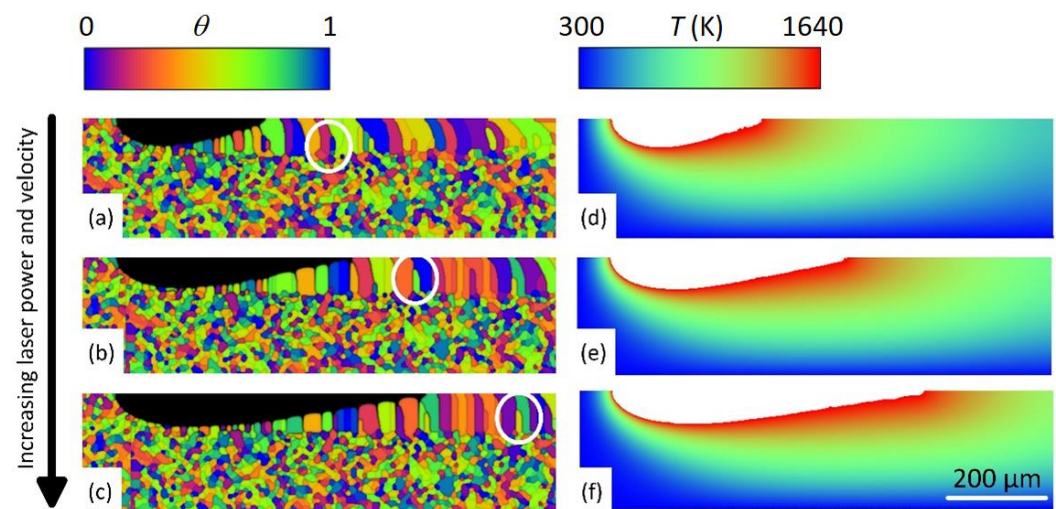


Figure 7. Simulated grain structure (left column) and temperature distribution (right column) in laser processing of Ni-0.2Al alloy. The dark areas in the left column indicate the liquid phase and the white areas in the right column indicate temperatures above 1640 K; (a,d) $p = 15 \text{ GW/m}^2$, $v_{\text{scan}} = 0.5 \text{ m/s}$; (b,e) $p = 21 \text{ GW/m}^2$, $v_{\text{scan}} = 0.7 \text{ m/s}$; (c,f) $p = 27 \text{ GW/m}^2$, $v_{\text{scan}} = 0.9 \text{ m/s}$.

The corresponding concentration and long-range order (LRO) parameter fields are illustrated in Figure 8a–c and 8d–f, respectively. The results indicate that the distribution of the alloying element (Al) in the re-solidified zone changes with the change in process parameters. Increasing the scan velocity appears to change the Al content at the grain boundaries. However, a more extensive parameter study and statistical analysis will be needed to verify this trend to establish a quantitative correlation between segregation pattern and processing conditions. Surface segregation of Ni is also observed in these cases. In addition to the re-solidified zone, the concentration distribution in the HAZ is changed during the process; the distribution of Al is more uniform in HAZ as compared to the base metal. Figure 8e–f shows how the initial distribution of the ordered Ni-rich phase (white points in the figure, representing Ni_3Al) changes during the laser treatment. The formation of a row of the ordered phase is observed at the bottom of the re-solidified zone. Increasing scanning velocity also leads to the formation of some ordered phases inside the columnar grains, as indicated in Figure 8f. In the HAZ, a decrease in the total volume of ordered phases is observed. As would be expected, increasing the scanning velocity decreases HAZ area. These results demonstrate the capability of the computational framework in capturing some key microstructural features, in addition to grain structure, during laser processing of an intermetallic forming system. Although further work will be required to verify the results of continuous melting, the findings are generally consistent with the existing understanding of the solidification behaviour of intermetallic forming systems. For instance, the absence of the ordered phase in the melt zone can be attributed to the generally sluggish growth of intermetallic phases [26] which can lead to their elimination during competitive phase selection. There is an indication of the dissolution of the ordered phase in the HAZ, which is extended far beyond that measure on the changes in the grain structure. Dissolution of small precipitates would be expected to have faster kinetics in a system where grains are pinned by a second phase at their boundaries.

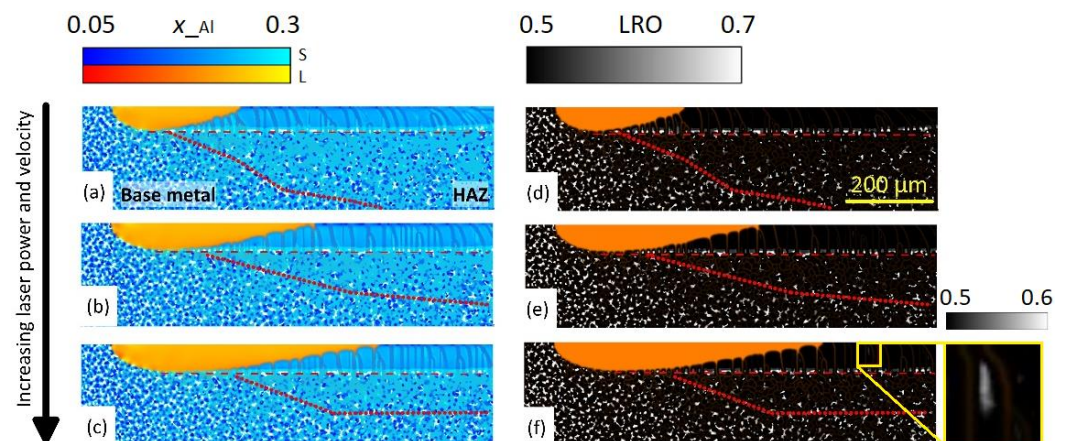


Figure 8. Simulated concentration distribution (left column) and long-range order parameter (right column) in laser processing of Ni-0.2Al alloy. The white points in the right column indicate ordered phases. Dotted lines indicate the approximate boundary of the HAZ (phase). Dashed lines show the boundaries between the re-solidified zone and the HAZ. The inset in (f) indicates an ordered phase in the re-solidified zone. (a,d) $p = 15 \text{ GW/m}^2$, $v_{\text{scan}} = 0.5 \text{ m/s}$; (b,e) $p = 21 \text{ GW/m}^2$, $v_{\text{scan}} = 0.7 \text{ m/s}$ (c,f); $p = 27 \text{ GW/m}^2$, $v_{\text{scan}} = 0.9 \text{ m/s}$.

4. Conclusions

Segregation of solute elements during pulsed laser surface melting of the Ni-Al intermetallic phase has been studied using a phase-field method, particularly tailored to capture the unusual kinetic effects during rapid solidification of phases with chemical long-range order. The results showed complex segregation patterns in the melted zone, which is attributed to the complex interplay of the variable solidification velocity in laser processing and the non-monotonic velocity-dependent partitioning of the solidifying intermetallic phase. When the kinetic effects are prominent, the employed phase-field method can show these complicated segregation patterns as observed previously in laser-processed single crystals of Ni-Al.

The results also demonstrated possible microstructural features that can arise during laser processing of polycrystalline Ni-rich alloys in the Ni-Al system, including dissolution of precipitates and the segregation pattern, in addition to a strongly textured grain structure. The computational methods presented in this study can serve as a basis to provide additional insight to the evolution of microstructure in laser processing of intermetallic containing systems, where unusual kinetic effects are likely to be present and significant.

Author Contributions: Conceptualization, M.A.J. and H.A.; methodology, H.A.; validation, M.A.J.; investigation, M.A.J.; writing—original draft preparation, M.A.J.; writing—review and editing, H.A.; visualization, M.A.J. All authors have read and agreed to the published version of the manuscript.

Funding: This research received no external funding.

Data Availability Statement: The data presented in this study are available on request from the corresponding authors.

Conflicts of Interest: The authors declare no conflict of interest.

References

- Birmingham, M.J.; StJohn, D.H.; Krynen, J.; Tedman-Jones, S.; Dargusch, M.S. Promoting the columnar to equiaxed transition and grain refinement of titanium alloys during additive manufacturing. *Acta Mater.* **2019**, *168*, 261–274. [[CrossRef](#)]
- Haines, M.; Plotkowski, A.; Frederick, C.L.; Schwalbach, E.J.; Babu, S.S. A sensitivity analysis of the columnar-to-equiaxed transition for Ni-based superalloys in electron beam additive manufacturing. *Comput. Mater. Sci.* **2018**, *155*, 340–349. [[CrossRef](#)]
- Liu, P.; Wang, Z.; Xiao, Y.; Horstemeyer, M.F.; Cui, X.; Chen, L. Insight into the mechanisms of columnar to equiaxed grain transition during metallic additive manufacturing. *Addit. Manuf.* **2019**, *26*, 22–29. [[CrossRef](#)]

4. Chandramohan, P. Laser additive manufactured Ti-6Al-4V alloy: Texture analysis. *Mater. Chem. Phys.* **2019**, *226*, 272–278. [[CrossRef](#)]
5. Lewandowski, J.J.; Seifi, M. Metal Additive Manufacturing: A Review of Mechanical Properties. *Annu. Rev. Mater. Res.* **2016**, *46*, 151–186. [[CrossRef](#)]
6. Kok, Y.; Tan, X.P.; Wang, P.; Nai, M.L.S.; Loh, N.H.; Liu, E.; Tor, S.B. Anisotropy and heterogeneity of microstructure and mechanical properties in metal additive manufacturing: A critical review. *Mater. Des.* **2018**, *139*, 565–586. [[CrossRef](#)]
7. Carroll, B.E.; Palmer, T.A.; Beese, A.M. Anisotropic tensile behavior of Ti-6Al-4V components fabricated with directed energy deposition additive manufacturing. *Acta Mater.* **2015**, *87*, 309–320. [[CrossRef](#)]
8. Li, J.; Zhou, X.; Brochu, M.; Provatas, N.; Fiona, Y. Solidification microstructure simulation of Ti-6Al-4V in metal additive manufacturing: A review. *Addit. Manuf.* **2020**, *31*, 100989. [[CrossRef](#)]
9. Frazier, W.E. Metal additive manufacturing: A review. *J. Mater. Eng. Perform.* **2014**, *23*, 1917–1928. [[CrossRef](#)]
10. Cherry, J.A.; Davies, H.M.; Mehmood, S.; Lavery, N.P.; Brown, S.G.R.; Sienz, J. Investigation into the effect of process parameters on microstructural and physical properties of 316L stainless steel parts by selective laser melting. *Int. J. Adv. Manuf. Technol.* **2015**, *76*, 869–879. [[CrossRef](#)]
11. Pekok, M.A.; Setchi, R.; Ryan, M.; Han, Q.; Gu, D. Effect of process parameters on the microstructure and mechanical properties of AA2024 fabricated using selective laser melting. *Int. J. Adv. Manuf. Technol.* **2021**, *112*, 175–192. [[CrossRef](#)]
12. Zhao, X.; Chen, J.; Lin, X.; Huang, W. Study on microstructure and mechanical properties of laser rapid forming Inconel 718. *Mater. Sci. Eng. A* **2008**, *478*, 119–124. [[CrossRef](#)]
13. Ram, G.D.J.; Reddy, A.V.; Rao, K.P.; Reddy, G.M. Control of laves phase in inconel 718 GTA welds with current pulsing. *Sci. Technol. Weld. Join.* **2004**, *9*, 390–398. [[CrossRef](#)]
14. Jabbareh, M.A.; Assadi, H. Modeling of Grain Structure and Heat-Affected Zone in Laser Surface Melting Process. *Metall. Mater. Trans. B* **2013**, *44*, 1041–1048. [[CrossRef](#)]
15. Karayagiz, K.; Johnson, L.; Seede, R.; Attari, V.; Zhang, B.; Huang, X.; Ghosh, S.; Duong, T.; Karaman, I.; Elwany, A.; et al. Finite interface dissipation phase field modeling of Ni–Nb under additive manufacturing conditions. *Acta Mater.* **2020**, *185*, 320–339. [[CrossRef](#)]
16. Wang, X.; Liu, P.W.; Ji, Y.; Liu, Y.; Horstemeyer, M.H.; Chen, L. Investigation on Microsegregation of IN718 Alloy during Additive Manufacturing via Integrated Phase-Field and Finite-Element Modeling. *J. Mater. Eng. Perform.* **2019**, *28*, 657–665. [[CrossRef](#)]
17. Radhakrishnan, B.; Gorti, S.B.; Turner, J.A.; Acharya, R.; Sharon, J.A.; Staroselsky, A.; El-wardany, T. Phase Field Simulations of Microstructure Evolution Laser Powder Bed Fusion. *Metals* **2019**, *9*, 14. [[CrossRef](#)]
18. Geng, R.; Du, J.; Wei, Z.; Ma, N. Multiscale modelling of microstructure, micro-segregation, and local mechanical properties of Al-Cu alloys in wire and arc additive manufacturing. *Addit. Manuf.* **2020**, *36*, 101735. [[CrossRef](#)]
19. Ghosh, S. Predictive modeling of solidification during laser additive manufacturing of nickel superalloys: Recent developments, future directions. *Mater. Res. Express* **2018**, *5*, 012001. [[CrossRef](#)]
20. Korner, K.; Markl, M.; Koepf, J.A. Modeling and Simulation of Microstructure Evolution for Additive Manufacturing of Metals: A Critical Review. *Metall. Mater. Trans. A* **2020**, *51*, 4970–4983. [[CrossRef](#)]
21. Mede, T.; Kocjan, A.; Paulin, I.; Godec, M. Numerical mesoscale modelling of microstructure evolution during selective laser melting. *Metals* **2020**, *10*, 800. [[CrossRef](#)]
22. Herlach, D.M.; Galenko, P.K. Rapid solidification: In situ diagnostics and theoretical modelling. *Mater. Sci. Eng. A* **2007**, *449–451*, 34–41. [[CrossRef](#)]
23. Assadi, H. A phase-field model for non-equilibrium solidification of intermetallics. *Acta Mater.* **2007**, *55*, 5225–5235. [[CrossRef](#)]
24. Assadi, H.; Reutzel, S.; Herlach, D.M. Kinetics of solidification of B2 intermetallic phase in the Ni–Al system. *Acta Mater.* **2006**, *54*, 2793–2800. [[CrossRef](#)]
25. Assadi, H.; Barth, M.; Greer, A.L.; Herlach, D.M. Kinetics of solidification of intermetallic compounds in the Ni–Al system. *Acta Metall.* **1998**, *46*, 491–500. [[CrossRef](#)]
26. Assadi, H.; Greer, A.L. Site-ordering effects on element partitioning during rapid solidification of alloys. *Nature* **1996**, *383*, 150–152. [[CrossRef](#)]
27. Greer, A.L.; Assadi, H. Rapid solidification of intermetallic compounds. *Mater. Sci. Eng. A* **1997**, *226–228*, 133–141. [[CrossRef](#)]
28. Assadi, H.; Greer, A.L. Modeling of kinetics of solidification of intermetallic compounds. *Mater. Sci. Eng. A* **1997**, *226–228*, 70–74. [[CrossRef](#)]
29. Gaffet, F.; Pelletier, J.M.; Bonnet-Jobez, S. Laser surface alloying of Ni film on Al-based alloy. *Appl. Surf. Sci.* **1989**, *43*, 248–255. [[CrossRef](#)]
30. Liang, G.Y.; Li, C.L.; Su, J.Y. Segregation phenomena of laser alloyed Ni–Cr–Al coating Al–Si alloy. *Mater. Sci. Eng. A* **1997**, *224*, 173–176. [[CrossRef](#)]
31. Kundin, J.; Mushongera, L.; Emmerich, H. Acta Materialia Phase-field modeling of microstructure formation during rapid solidification in Inconel 718 superalloy. *Acta Mater.* **2015**, *95*, 343–356. [[CrossRef](#)]
32. Kumara, C.; Segerstark, A.; Hanning, F.; Dixit, N.; Joshi, S. Microstructure modelling of laser metal powder directed energy deposition of Alloy 718 Microstructure modelling of laser metal powder directed energy deposition of alloy 718. *Addit. Manuf.* **2018**, *25*, 357–364. [[CrossRef](#)]

33. Gong, T.; Chen, Y.; Li, S.; Cao, Y.; Hou, L.; Li, D.; Chen, X.-Q.; Reinhart, G.; Nguyen-Thi, H. Equiaxed dendritic growth in nearly isothermal conditions: A study combining in situ and real-time experiment with large-scale phase-field simulation. *Mater. Today Commun.* **2021**, *10*, 102467. [[CrossRef](#)]
34. Chen, Q.; Zhang, L.; Tang, S.; Liang, C.; Ma, Y.; Liu, W. Examination of dendritic growth and microsegregation during solidification of Al–Li binary alloy using the phase-field simulation coupling CALPHAD data. *Calphad Comput. Coupling Phase Diagr. Thermochem.* **2021**, *74*, 102271. [[CrossRef](#)]
35. Zhang, Y.; Xu, Q. Precipitation and growth simulation of γ' phase in single crystal superalloy DD6 with multiphasefield method and explicit nucleation algorithm. *Metals* **2020**, *10*, 1346. [[CrossRef](#)]
36. Assadi, H.; Oghabi, M.; Herlach, D.M. Influence of ordering kinetics on dendritic growth morphology. *Acta Mater.* **2009**, *57*, 1639–1647. [[CrossRef](#)]
37. Iida, T.; Guthrie, R.I.L. *The Physical Properties of Liquid Metals*; Clarendon Press: Oxford, UK, 1988.
38. Nikbakht, R.; Assadi, H. Phase-field modelling of self-propagating high-temperature synthesis of NiAl. *Acta Mater.* **2012**, *60*, 4041–4053. [[CrossRef](#)]
39. Kurz, W.; Trivedi, R. Banded solidification microstructures. *Metall. Mater. Trans. A* **1996**, *27A*, 625–634. [[CrossRef](#)]